Large-eddy simulation of shock/boundary-layer interaction

By A. Hadjadj†, J. Larsson, B. E. Morgan, J. W. Nichols AND S. K. Lele

This work considers numerical simulations of supersonic flows when shock/turbulent boundary layer interaction occurs. Such flows reveal the existence of complex mechanisms, which need to be carefully investigated for efficient design of propulsion systems. In this study, large-eddy simulation is used to investigate unsteady mechanisms. Since a shock-capturing scheme is used, a hybrid numerical scheme has been developed to reduce its dissipative properties. The issue of the generation of coherent turbulent inlet boundary conditions is also addressed. To avoid introducing artificial low-frequency modes that could affect the interaction, a method based on a digital-filter approach originally developed by Klein *et al.* (2003) and modified by Xie & Castro (2008) and Touber & Sandham (2009) is used to provide a synthetic-inflow condition over a relatively short distance. The obtained results are analyzed and discussed in terms of mean and turbulent quantities. Excellent agreement between LES and experimental data is obtained for both the undisturbed boundary layer and the shock impingement region. In the latter case, oscillations of the reflected shock occurring at low frequencies are observed, in agreement with previous numerical and experimental findings. Moreover, simulations reveal the presence of such frequencies mainly near the shock foot and within the recirculation bubble. This point gives credit to the hypothesis that the instabilities of the reflected shock are due to the intrinsic low-frequency movement of the shock/bubble acting dynamically as a coupled system.

1. Background & Motivation

The interaction of shock waves with boundary layers is a basic fluid-dynamics phenomenon that has both fundamental and practical importance. From the engineering viewpoint, this problem can have a significant influence on aircraft or rocket performance and often leads to extremely undesirable effects, such as drag rise, massive flow separation, shock unsteadiness and high wall heating. From the fundamental point of view, this phenomenon represents one of the simplest flow configurations yielding a strong viscous/inviscid interaction, and is therefore an ideal test case for Navier-Stokes solvers. In this problem, several viscous phenomena are observed, including a boundary layer with adverse pressure gradients, induced separation, shear layers, and a recirculation bubble; some of the salient features of these phenomena are given by Dolling (2011); Settles & Dolling (1990); Délery & Marvin (1996); Dolling & Dussauge (1989).

Previous studies on supersonic bounded flows (Kistler 1964; Erengil & Dolling 1991; Baresh *et al.* 2002; Kim & Sung 2006; Hou *et al.* 2004; Ganapathisubramani *et al.* 2007) have shown that shock-wave/boundary-layer interactions occurring in many situations, such as ducts, wind tunnels, nozzles or ramps, may exhibit strong unsteadiness that causes large shock excursions associated with amplified wall-pressure fluctuations. These

† National Institute of Applied Sciences, INSA of Rouen & CORIA UMR 6614 CNRS, France
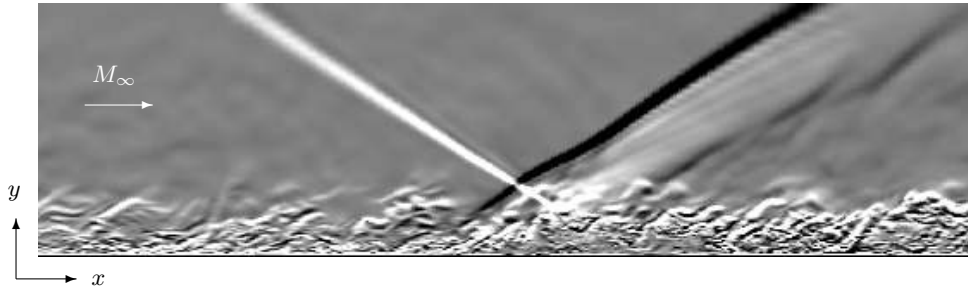
FIGURE 1. Instantaneous numerical schlieren picture of an oblique shock impinging on a turbulent boundary layer at $M_\infty = 2.28$ and $Re_\theta \simeq 5350$. The incoming boundary layer has a thickness of $\delta = 10.83$ mm, with an incident-shock angle $\beta = 32.41°$ and a wedge deflection $\theta = 8°$. This image is based on the instantaneous density-gradient field, extracted from the present LES computation.

studies have shown that the shock motion has a frequency much lower than the characteristic frequency of the turbulent boundary layer, and that the time scale associated with the low frequency is $\mathcal{O}(10\delta/U_\infty - 100\delta/U_\infty)$, in contrast to the characteristic time scale of the incoming boundary layer, which is $\mathcal{O}(\delta/U_\infty)$. Despite a large number of experimental and numerical studies devoted to the characterization of shock oscillations and large-scale turbulence identification, the cause of the low-frequency motion (influence of upstream or downstream conditions or intrinsic shock low-pass filter behavior) is still an open question.

From a numerical point of view, significant progress has been made in the development of both steady (RANS) or unsteady hybrid (RANS/LES) methods, which incorporate configuration-dependent flow physics. In general, the majority of RANS models fail to capture the high level of unsteadiness in the shock system observed in the experiments and they don't provide a good prediction of root-mean-square (r.m.s.) pressure and heat transfer fluctuations at the surface. Recently, however, large-eddy simulation (LES) and direct numerical simulations (DNS) have been applied to the SWBLI problem with significant success (Adams 2000; Garnier & Sagaut 2002) and subsequently some tentative explanations of the origin of the low-frequency shock motion have been given by several authors (see for example, Pirozzoli & Grasso 2006; Wu & Martin 2008; Touber & Sandham 2009).

The present work focuses on the use of large-eddy simulations for the study of an oblique shock interacting with turbulent boundary layer over an adiabatic flat plate (see Figure 1). To provide more insight into the computed results, the experimental data provided by Deleuze (1995); Laurent (1996) and more recently by Debiève & Dupont (2009) are used to study the unsteady aspects of the 3D SWBLI, with particular emphasis on the origin of the low-frequency oscillations associated with wall pressure fluctuations. The paper also briefly addresses the important question of the three-dimensionality of the flow in the presence of side walls, and the possible effect of the spanwise confinement on the flow organization together with the associated low-frequency unsteadiness.

2. Numerical procedure and LES methodology

In addition to the sub-grid scale modeling, another issue of the LES technique is the choice of the numerical method. Modern low-dissipative high-order methods, based on Riemann solvers and high-order WENO interpolations, are now generally regarded
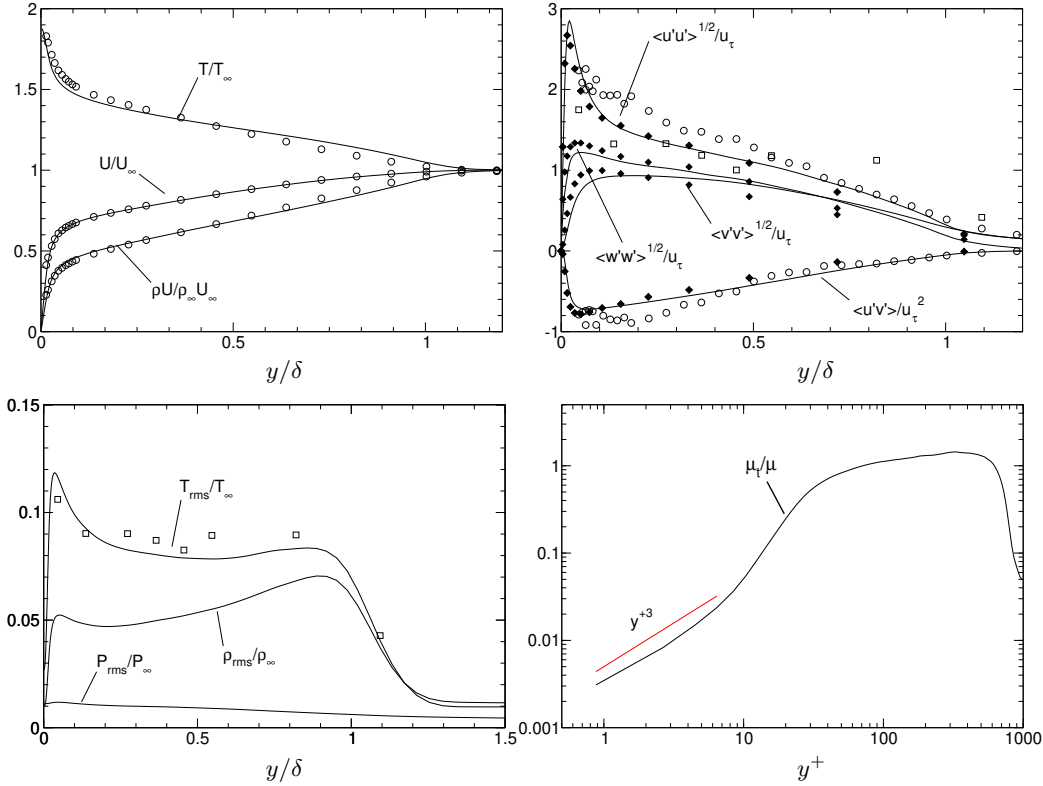
FIGURE 2. Wall-normal distributions of first- and second-order turbulence statistics of the incoming boundary layer. ——, LES; ○, Laser Doppler Anemometry (LDA); □, Hot-Wire Anemometry (HWA); ◆, DNS (Pirozzoli *et al.* 2004).

as offering an accurate and stable numerical framework. However, several studies (see Mittal & Moin 1997; Garnier *et al.* 1999) indicated that these high-order shock-capturing schemes are still much too dissipative to capture fine-scale turbulence fluctuations. This has encouraged the hybridization between spectral or high-order compact schemes and high-resolution shock-capturing methods, where a flow sensor is used to switch to shock-capturing methods at discontinuities (see Hill & Pullin 2004; Pantano *et al.* 2007; Touber & Sandham 2009). Accordingly, in this study a fifth-order WENO scheme combined with a centered fourth-order scheme is used to calculate the convective fluxes, via the selective Ducros' sensor. Viscous terms are discretized using a centered fourth-order accurate scheme, while an explicit third-order Runge-Kutta method of Shu and Osher is used for time integration. In this study, the dynamic procedure of Germano *et al.* (1991) and Lilly (1962) is used. The turbulent heat flux is modeled with a gradient transport model, including a variable turbulent Prandtl number (Moin *et al.* 1991). Concerning the inflow boundary conditions, an existing method for the generation of unsteady compressible turbulent boundary layers, based on a digital filter approach, is used. The main advantage of this method over the recycling/rescaling approach or the forced laminar-to-turbulent transition technique is to allow the simulation to generate its own coherent inflow data
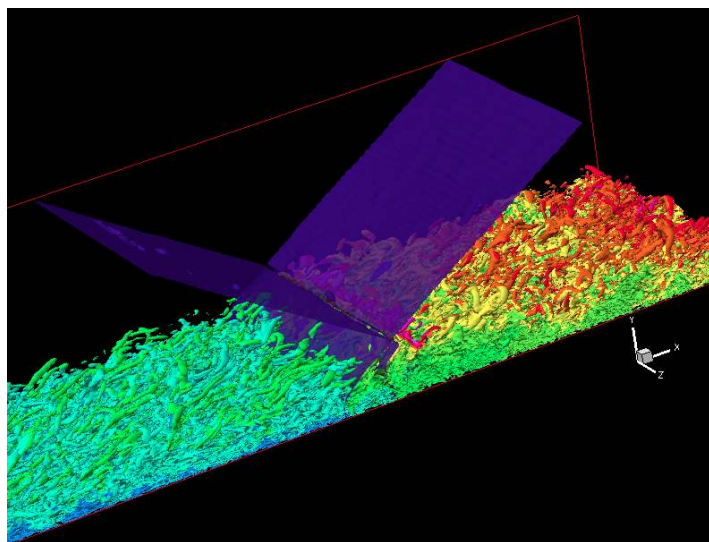
FIGURE 3. Instantaneous iso-surface of the second invariant of the velocity gradient tensor $Q = 0.01Q_{max}$ colored by the density field.

without introducing any particular mode into the computational domain (in particular the low-frequency one) which may interact with the shock/boundary-layer system. The detailed procedure of this method can be found in Touber (2010).

3. Results and discussion

3.1. *Supersonic incoming boundary layer*

We first report some of the characteristics of the supersonic incoming boundary layer (in the absence of interacting shock), which evolves at $M_\infty = 2.28$ and has a momentum-thickness Reynolds number of $R_{e_\theta} \simeq 5350$. The size of the computational domain is $L_x \approx 15\,\delta_{in}$, $L_y \approx 6.5\,\delta_{in}$, $L_z \approx 5\,\delta_{in}$, where $\delta_{in} = 10.83$ mm is the incoming boundary-layer thickness. Note that the spanwise length was varied from $\sim \delta_{in}$ (narrow domain) to $5\,\delta_{in}$ (wide domain) to cover roughly half of the wind-tunnel extent. The two-point autocorrelation coefficients in the homogeneous direction (z) for both cases (narrow and wider domains) are examined. Results (not presented here for brevity) show that the decorrelation of velocity and pressure fluctuations is achieved over a distance of $L_z/2$ for both narrow and wide domains, which indicates that the turbulence dynamics are not inhibited. Basically, in terms of turbulence statistics, no significant differences were found between the two different domain extents. This suggests that the narrow-span LES is in general sufficient to resolve most of the features occurring in boundary layers. However, as will be discussed later, the variation of the spanwise length may significantly affect the predicted interaction lengths and the associated low-frequency unsteadiness. In what follows, only results of the wider domain will be presented and discussed. In this case, the mesh contains 10^7 grid points and is stretched in the wall-normal direction with more clustering in the boundary layer. In wall units, the closest grid point to the wall is at $\Delta y_{min}^+ \simeq 1$ (the superscript + indicates usual normalization by the friction velocity, with $y^+ = \rho_w\, y\, u_\tau/\mu_w$, where μ_w and ρ_w are the dynamic viscosity and the density at the wall, respectively). In the streamwise and spanwise directions, the mesh resolution gives
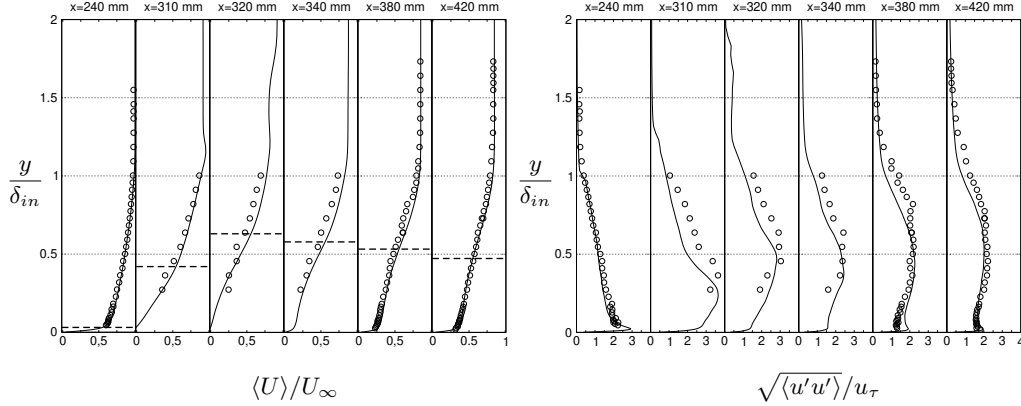
FIGURE 4. Longitudinal mean and fluctuating velocity profiles vs. y/δ_{in} in the upstream boundary layer and along the interaction region. ——, LES; ○, Laser Doppler Anemometry (LDA); - - -, sonic line.

cell sizes in wall units of $\Delta x^+ = 40$ and $\Delta z^+ = 16$, respectively. As a first step, the flow is assumed to be homogeneous in the spanwise direction, so that periodic boundary conditions are retained. The examination of the instantaneous three-dimensional iso-vorticity field shows that the boundary layer is fully developed and self preserving. Also, the simulation reveals the appearance of large-scale motion in the outer region of the boundary layer, dominated by the entrainment process. These large-scale structures are particularly active near the edge of the boundary layer, where they remain coherent long enough so that they are strongly responsible for the intermittency of the boundary layer and its growth rate. The reported turbulence statistics are examined to evaluate their consistency with both DNS (Pirozzoli *et al.* 2004) and measurements (Deleuze 1995; Laurent 1996). They are based on time-averaging of the instantaneous three-dimensional fields that are extracted from a time series covering 200 characteristic times, $\tau_c = \delta_{in}/U_\infty$. As shown in Figure 2, the LES results match well with both DNS and experimental data. It is worth noting that the near-wall behavior of the subgrid viscosity is well recovered ($\mu_t \sim y^{+3}$), showing that the current subgrid modeling, which does not incorporate any information related to the location of the solid walls, is well suited for the simulation of bounded turbulent flows.

3.2. *Shock/boundary-layer interaction*

Considering the shock-boundary layer interaction problem, the computations are performed based on the test case studied experimentally by the IUSTI group in Marseille. The shock generator has an angle of $\theta = 8°$, which corresponds to an oblique shock of $32.41°$ inclination at Mach 2.28. The incoming boundary condition is extracted from the data of the spatially-developing boundary layer discussed in the previous section. The size of the computational domain is nearly the same, except for an extension made in both x and y directions to cover both the interaction zone and the relaxation region. This is to avoid a possible confinement of the shock system in the cross-streamwise direction. An extensive grid refinement was performed in order to achieve an improvement in the predicted flow both with respect to the separation and the reattachment positions. The final mesh contained $N_x \times N_y \times N_z = 375 \times 160 \times 461$ points, covering
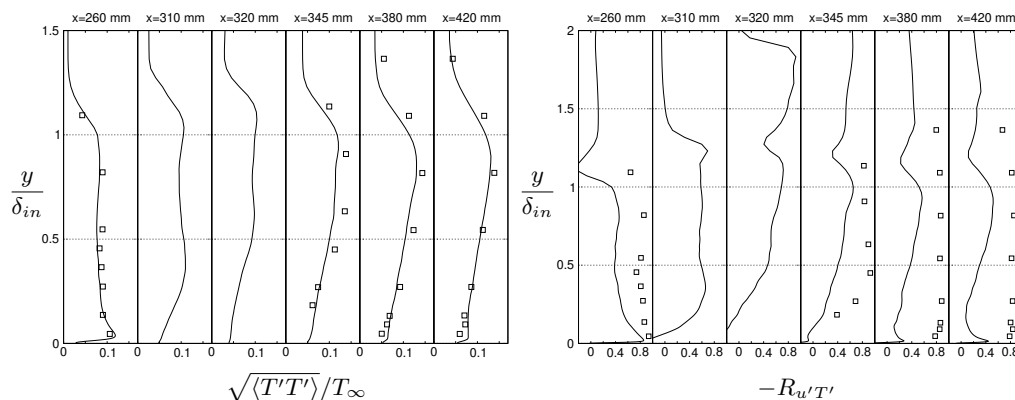
FIGURE 5. Temperature fluctuation and $-R_{u'T'}$ correlation. ——, LES; ▫, Exp. (HWA).

$L_x \times L_y \times L_z = 20\delta_{in} \times 10\delta_{in} \times 5\delta_{in}$. It is important to notice that the presence of the shock wave poses a particular problem in LES. Indeed, the sub-grid viscosity ratio, μ_t/μ, may exhibit high values near discontinuities, even outside of the boundary layer. This result is not surprising since the amount of sub-grid viscosity evolves proportionally to the second invariant of the deformation tensor. Thus, the resolved turbulence can be artificially damped when crossing the shock. To overcome this problem, the subgrid model was used only in the region of the flow where the centered scheme is active. In other words, the subgrid viscosity μ_t is set to zero when the WENO scheme is used. The methodology and the performance of this approach for shock/turbulence interaction is under investigation (Hadjadj *et al.* 2010).

3.2.1. *Instantaneous structures and mean properties*

The instantaneous iso-surface of the Q vortex-identification criterion, reported in Figure 3, reveals the existence of complex organized motion in the outer part of the boundary layer as well as in the interaction zone, which is characterized by the occurrence of large-scale structures that exhibit a highly intermittent character. At the interaction point, the incident shock bends toward the wall while penetrating the boundary layer and then is reflected back through the sonic line. The time-averaged flowfield exhibits a small recirculation bubble close to the wall, which is induced by the impingement of the incident shock onto the separated boundary layer. Later, the formation of an expansion fan followed by a series of compression waves helps the boundary layer to reattach to the wall and to relax further downstream. Figure 3 also demonstrates that the post-separation shear layer contains a coherent motion associated with the Kelvin-Helmholz-like vortices. This organized motion contributes directly to the turbulence level in the shear layer as well as interacts sensitively with the temporal variation of the separation process. The computed mean and fluctuating velocities at several measurement locations are shown in Figure 4. Throughout the interaction region, the computation shows in general close agreement with the experiments.

3.2.2. *Strong Reynolds Analogy*

The objective behind the analysis of the Strong Reynolds Analogy (SRA) is to test the departure from the common assumption in the specific case of shock/boundary layer
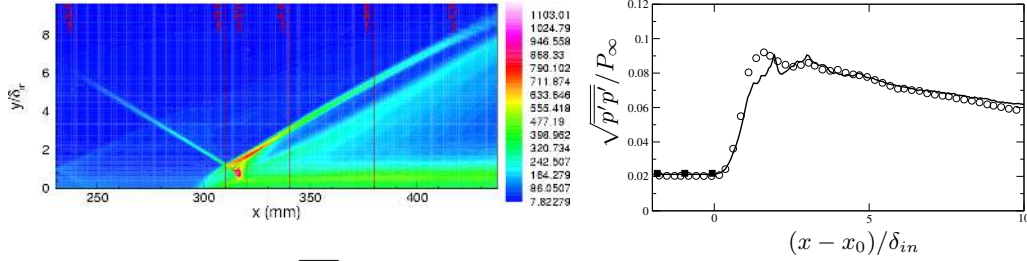
FIGURE 6. (left) Plot of $\sqrt{\overline{p'p'}}$ (Pa), (right) longitudinal distribution of *r.m.s.* wall pressure normalized by the reference static pressure. ——, LES; ○, LES-L4 provided by Pirozzoli & Bernardini during the CTR Summer Program 2010, ■; ratio of *r.m.s.* of wall pressure to free-stream static pressure in the undisturbed boundary layer ($p_{rms} \simeq 2.5\,\tau_w$, where τ_w is the wall-shear stress, see Willmarth & Yang (1970)). Note that the origin of the x-axis corresponds to the beginning of the interaction zone, whose length is $L \simeq 3\,\delta_{in}$, with a corresponding separation length $L_{sep} \simeq 2.34\,\delta_{in}$.

interaction, and to verify the applicability of Morkovin's hypothesis. Reynolds analogies in supersonic flows imply that the total temperature fluctuations are negligible and the turbulent Prandtl number is one. In particular, this yields to the following relations:

$$SRA = \frac{\sqrt{\langle T'T' \rangle}/\widetilde{T}}{(\gamma - 1)\langle M \rangle^2 \sqrt{\langle u'u' \rangle}/\widetilde{u}} \approx 1, \qquad R_{u'T'} = \frac{\langle u'T' \rangle}{\sqrt{\langle u'^2 \rangle \langle T'^2 \rangle}} \approx -1, \qquad (3.1)$$

where $\langle M \rangle = \langle u \rangle / \langle c \rangle$ is the local Mach number, where $\langle . \rangle$ implies time and space averages. As shown in Figure 5 (right), the relations (3.1) are not valid in the boundary layer as well as in the interaction and the relaxation regions. For instance, the value of the measured correlation coefficient $-R_{u'T'}$ is less than unity (≈ 0.85) in most of the flow. In addition, DNS data of supersonic boundary layers (Pirozzoli *et al.* 2004; Guarini *et al.* 2000) have shown that this coefficient remains close to 0.60 throughout most of the boundary layer and exhibits a maximum value of 0.84 when approaching the wall. In this case, both DNS and LES reproduce the same trend, except in the outer part of the boundary layer where the correlation coefficient falls to 0.45 for LES. As suggested by Gaviglio (1991), discrepancies observed between experiments and simulations may be due to a difference in the magnitude of the acoustic field which is not the same in the computation as in the blowdown wind tunnel. Furthermore, these results confirm that the fluctuations of the total temperature are not negligible and the strong Reynolds analogy (SRA) is no longer valid either in the boundary layer or in the post-shock interaction region.

3.2.3. *Analysis of SWBLI unsteadiness*

The problem of shock unsteadiness at low frequency, relative to the higher characteristic frequency of the incoming turbulent boundary layer, is somehow related to the dynamics of the separated bubble, that pulsates the whole shock system and causes global unstable movement, generally leading to strong expansions and contractions of the flow field in a breathing motion. Also, the boundary-layer separation gives rise to a detached shear layer that convects the perturbations far downstream. The associated shedding phenomenon is known to generate strong coupling between the shock region and the downstream relaxation zone. Figure 6 (left) displays contours of *r.m.s* pressure, $p_{rms} = \sqrt{\overline{p'p'}}$. It can be seen that the amplification of pressure fluctuations is much more important in the interaction zone and in the downstream relaxation region (6% to 7% of $P_{\infty,in}$) compared to the upstream boundary layer, which exhibits a lower level (2% of
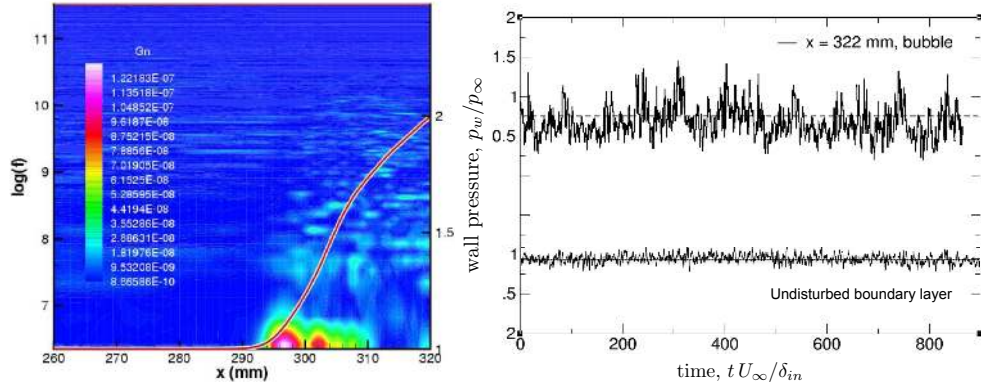
FIGURE 7. (left) Power Spectral Density (PSD) of wall-pressure fluctuations normalized using its local integral, plotted with the mean profile of the wall pressure (red line). (right) Instantaneous long time wall-pressure signals taken upstream of the interaction and at the recirculation zone.

$P_{\infty,in}$). This behavior is clearly visible in the wall-pressure distribution (Figure 6, right), which shows higher values of $\sqrt{\overline{p'p'}}$ near the reflected shock. In accordance with recent experimental observations (Dupont *et al.* 2006), one can attribute this amplification to the unsteady behavior of the separated shock system. In the same way, the foot of the incident shock, supported by the sonic line, exhibits strong fluctuations, which possibly result from oscillations of the recirculation bubble, as mentioned before.

Power Spectral Density (PSD) of wall-pressure fluctuations is shown in Figure 7 along with the long-time wall-pressure history. The colored field represents spatial distribution of iso-PSD $(x, log(F))$ normalized by its local integral, $G_n(F)$. This normalization has the advantage of better highlighting the contribution of each frequency at a given co-ordinate x, with: $\int_0^\infty G_n(f)\, df|_x = 1$. The average wall-pressure profile is also reported in the same figure to help localize the compression waves acting on the shock foot. An energy accumulation at low frequencies is observed at $295\, mm < x < 310\, mm$ (including a part of the separated zone), which reveals the existence of a low-frequency movement of the reflected shock ($< 1kHz$ and $S_t \approx 0.02$. Here, the Strouhal number is defined as $S_t = fL_{sep}/U_\infty$).

This observation is in agreement with experimental investigations, which emphasizes a dominant frequency, associated with the shock movement, of $350\, Hz\, (S_t \approx 0.01)$. It is worth noticing that the highest energy contribution is located at the beginning of the separation zone ($295\, mm < x < 300\, mm$), whereas energies associated with frequencies lower than $1kHz$ are very weak in the upstream boundary layer as well as in the central part of the recirculation zone ($x = 315\, mm$). It seems, however, that low-frequency phenomena reappear at the end of the recirculation zone ($x = 320\, mm$). For further investigations of shock oscillations, PSD of surface pressure fluctuations, conditioned by the average shock position, at the outer part of the boundary layer ($x = 322\, mm$ and $y = 16.8\, mm$, for $y_{in}^+ = 1150$), are examined. Results (not shown here for concision) show clearly that high energies are associated with frequencies lower than $1\, kHz$, confirming experimental evidence of low-frequency shock oscillations. PSD signals of $\rho u'$ are also analyzed. Again, we notice an energy accumulation associated with a low-frequency unsteadiness of the recirculation bubble ($< 1kHz$), featuring similarities with the movement of the reflected shock.
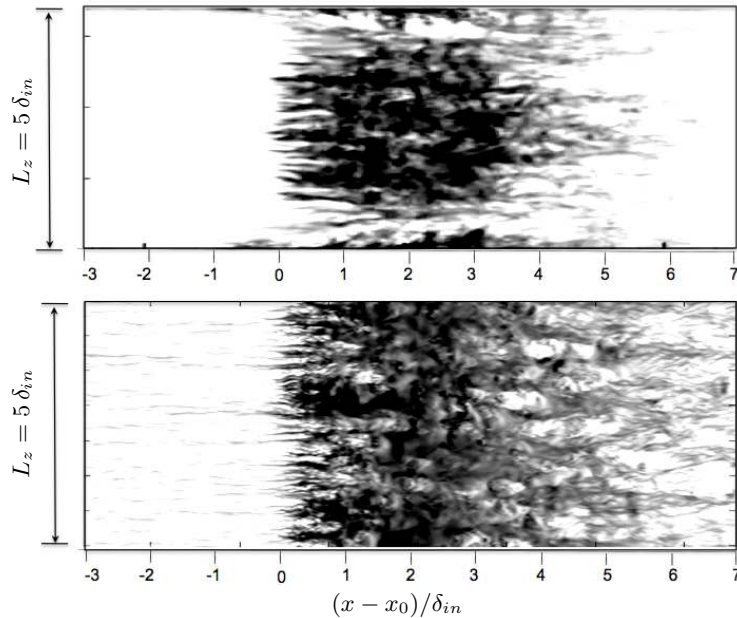
FIGURE 8. Instantaneous snapshot of u'/U_∞ at $y^+ = 10$ with two different spanwise boundary conditions; (top) slip condition, (bottom) periodic condition.

Finally, Figure 8 highlights the importance of the spanwise boundary conditions on the global flow organization in general and on the interaction zone and the reversal flow in particular. Due to the limitation on the CPU time and computer memory, the boundary layer on the side walls was not solved. Instead, we have assumed lateral slip boundaries with reflecting boundary conditions. The idea behind this is to confine the flow, by keeping the total mass flow constant. In order to help stabilize the flow, the turbulent velocity fluctuations in the spanwise directions were damped and a boundary layer-like profiles are specified at the inlet boundary along the side walls to avoid singularity. The main difference between the two computations is observed downstream of the interaction, where the bubble contour of the confined case exhibits two small near-wall vortices, which closely resemble the experimental results. In addition, one must recall that the shape of the separation bubble depends on the spanwise length and therefore large streamwise structures may affect the shock front by producing spanwise wrinkles. The side-wall vortices are found to reduce the effective spanwise section and strengthen the interaction. We also found that the low-frequency energy content is greater in the confined case compared to the periodic one (see Figure 9). However, the relation between the corner-flow unsteadiness and the low-frequency motion of the main separation bubble is still an open question.

4. Conclusions

The major properties of the flow occurring when an incident oblique shock interacts with a flat plate turbulent boundary layer have been investigated using large-eddy simulations. The study mainly focuses on the unsteady aspects of the interaction, with particular emphasis on the origin of the low-frequency oscillations associated with wall-pressure fluctuations. It has been shown that the present LES does capture the important
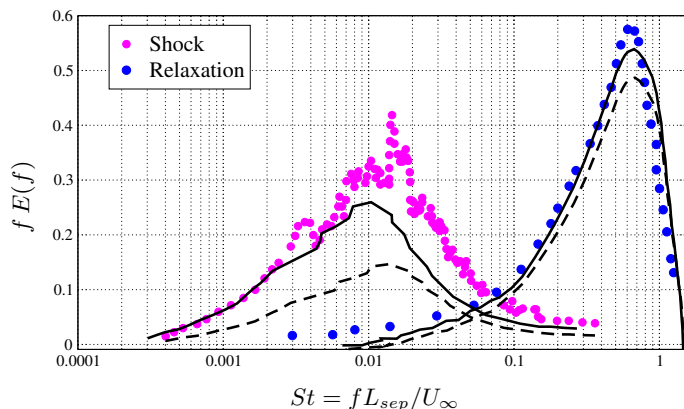
FIGURE 9. Spectral analysis of the wall-pressure signals near the shock and far downstream in the relaxation zone. Premultiplied power-spectral density. ———, LES-slip-walls taken at the centerline of the computational domain, $L_z/2$; - - -, LES-periodic; •/•, Experimental data (Dupont *et al.* 2003).

dynamics of this interaction: namely, the frequency of the most energetic low-frequency unsteadiness and the bandwidth of the low-frequency content. Another important point highlighted in this paper is the effect of side walls on the flow characteristics including the shock structure, the separated flow region, and the low-frequency content associated with the wall-pressure fluctuations. In this study, full validation of the numerical data has been achieved through systematic CFD/experiment comparison. This verification step is important because it helps to provide an estimate of the accuracy of the modeling. In this regard, it has been shown that the LES accurately predicts the mean temperature and density profiles, wall pressure, root-mean-square of velocity, temperature fluctuations and Reynolds shear stress profiles. In agreement with both DNS and experimental data, this study also shows that the streamwise velocity component and the temperature are weakly anti-correlated ($-R_{u'T'} \approx 0.5$). Experimental evidence suggests, however, a higher value of the correlation coefficient than the one found in the simulation. In this case, fluctuations of the total temperature are not negligible and the strong Reynolds analogy (SRA) is not valid. Finally, oscillations of the reflected shock occurring at low frequencies are observed, in agreement with previous numerical and experimental investigations. Simulations reveal the presence of such frequencies mainly downstream of the shock and near the recirculation bubble. The fact that the low frequencies of the shock/bubble system persist, even in the absence of upstream low-frequency forcing, would therefore seem to suggest that they are not due to a low-pass filtering effect. Rather, they must be a consequence of the intrinsic dynamics of the system (in the sense of a global mode). Although basic understanding of flow physics of this interaction has been achieved through different numerical and experimental investigations, substantial additional research in full 3D shock-wave turbulent boundary layer interactions is still needed. The preliminary study of the confinement effects initiated during this summer program gives good scope for further investigations. In particular, if the structure of the interaction is strongly affected by the lateral walls, the shock will certainly accommodate with this complex three-dimensional organization and spanwise shock oscillations will

develop with different frequencies and wavelengths. Consequently, full characterization of the flowfield should be attempted by means of 3D simulations including lateral-wall effects, in conjunction with a global stability analysis that can be conducted in parallel.

Acknowledgments

REFERENCES

ADAMS, N.A. 2000 Direct simulation of the turbulent boundary layer along a compression ramp at $M = 3$ and $R_{e_\theta} = 1685$. *J. Fluid Mech.* **420**, 47–83.

BARESH, S.J., CLEMENS, N.T. & DOLLING, D.S. 2002 Relationship between upstream turbulent boundary-layer velocity fluctuations and separation shock unsteadiness. *AIAA J.* **40**(12), 2412–2422.

DEBIÈVE, J.F. & DUPONT, P. 2009 Dependence between the shock and the separation bubble in a shock wave boundary layer interaction. *Shock Waves* **19**, 163–169.

DÉLERY, J., MARVIN, J.G. 1996 Shock-wave boundary layer interactions. *AGARDograph* **280**.

DELEUZE, L. 1995 Structure d'une couche limite turbulente soumise à une onde de choc incidente. *Ph.D thesis, Université Aix-Marseille II, France.*

DOLLING, D., DUSSAUGE, J.P. 1989 Fluctuating wall-pressure measurements. *AGARDograph* **315**, NATO, Neuilly s/Seine.

DOLLING, D.S. 2001 Fifty years of shock-wave/boundary-layer interaction research: what next? *AIAA J.* **39**, 1517–1531.

DUPONT, P., DEBIÈVE, J.-F., DUSSAUGE, J. P, ARDISSONNE, J.P. & HADDAD, C. 2003 Unsteadiness in shock wave/boundary layer interaction. 2003 *Technical Report, ATAC working group*, ONERA, Sep. 18.

DUPONT, P., HADDAD, C. & DEBIÈVE, J.-F. 2006 Space and time organization in a shock-induced separated boundary layer. *J. Fluid Mech.* **559**, 255–277.

ERENGIL, M.E. & DOLLING, D.S. 1991 Unsteady wave structure near separation in a Mach 5 compression ramp interaction. *AIAA J.* **29**(5), 728–735.

GANAPATHISUBRAMANI, B., CLEMENS, N.T. & DOLLING, D.S. 2007 Effects of upstream boundary layer on the unsteadiness of shock-induced separation. *J. Fluid Mech.* **585**, 369–394.

GARNIER, E. & SAGAUT, P. 2002 Large eddy simulation of shock/boundary-layer interaction. *AIAA J.* **40**(10), 1935–1944.

GARNIER, E., MOSSI, M., SAGAUT, P., COMTE, P., DEVILLE, M. 1999 On the use of shock-capturing schemes for large-eddy simulation. *J. Comp. Phys.* **153**, 273–311.

GERMANO, M., PIOMELLI, U., MOIN, P. & CABOT, W. H. 1991 A dynamic subgrid-scale eddy viscosity model. *Phys. Fluids A 3*, 1760.

GAVIGLIO, J. 1987 Reynolds analogies and experimental study of heat transfer in the supersonic boundary layer. *Int. J. Heat Mass Transfer* **30**, 911–926.

GUARINI, S., MOSER, R., SHARIFF K., WRAY, A. 2000 Direct numerical simulation of a supersonic turbulent boundary layer at Mach 2.5. *J. Fluid Mech.*, **414**, 1–33.

HADJADJ, A., I. BERMEJO-MORENO & LARSSON, J. 2010 Note on filtering near shocks in large-eddy simulation. *CTR Annual Research Briefs.*

HILL, D.J. & PULLIN, D.I. 2004 Hybrid tuned center-difference-WENO method for large eddy simulations in the presence of strong shocks. *J. Comp. Phys.* **194** (2) 435–450.

HOU, Y.X., UNALMIS, O.H & BUENO, P.C. 2004 Effects of boundary-layer velocity fluctuations on unsteadiness of blunt-fin interactions. *AIAA J.* **42**(12), 2615–1219.

KIM, J. & SUNG, H.J. 2006 Wall pressure fluctuations in a turbulent boundary layer over a bump. *AIAA J.* **44**(7), 1393–1401.

KISTLER, A.L. 1964 Fluctuating wall pressure under a separated supersonic flow. *J. Acoustical Society of America* **36**(3), 543–550.

KLEIN, M., SADIKI, A. & JANICKA, J. 2003 A digital filter based generation of inflow data for spatially developing direct numerical or large eddy simulations. *J. Comp. Phys.*, **186**, 652–665.

LAURENT, H. 1996 Turbulence d'une interaction onde de choc/couche limite sur une paroi plane adiabatique ou chauffée. *Ph.D thesis, Université Aix-Marseille II, France.*

LILLY, D. K. 1992 A proposed modification of the Germano subgrid-scale closure method. *Phys. Fluids* **4**, 633–.

MITTAL, R., MOIN, P. 1997 Stability of upwind-based finite difference schemes for large-eddy simulation of turbulent flows. *AIAA J.* **35**, 1415–1417.

MOIN, P., SQUIRES, K., CABOT, W. & LEE, S. 1991 A dynamic subgrid-scale model for compressible turbulence and scalar transport. *Phys. Fluids* **11**, 2746–2757.

PANTANO, C., DEITERDING, R. HILL, D.J., PULLIN, D.I. 2007 A low numerical dissipation patch-based adaptive mesh refinement method for large-eddy simulation of compressible flows. *J. Comp. Phys.* **221**, 63–87.

PIROZZOLI, S., GRASSO, F. & GATSKI, T. B. 2004 Direct numerical simulation and analysis of a spatially evolving supersonic turbulent boundary layer at M=2.25. *Shock Waves* **16**, 530–545.

PIROZZOLI, S. & GRASSO, F. 2006 Direct numerical simulation of impinging shock wave/turbulent boundary layer interaction at M=2.25. *Phys. Fluids* **8**, 1–17.

SETTLES, G.S. & DOLLING, D.S. 1990 Swept shock wave/boundary layer interactions - Tutorial and update. *AIAA Paper 90-0375.*

TOUBER, E. 2010 Unsteadiness in shock-wave/boundary-layer interactions. *Ph.D Thesis*, University of Southampton, UK.

TOUBER, E. & SANDHAM, N. D. 2009 Large-eddy simulation of low-frequency unsteadiness in a turbulent shock-induced separation bubble. *Theor. Comput. Fluid Dyn.* **23**(2), 79–107.

WILLMARTH, W. & YANG, C.S. 1970 Wall-pressure fluctuations beneath turbulent boundary layers on a flat plate and a cylinder *J . Fluid Mech.* **41**, 47–80

WU, M. & MARTIN, M.P. 2008 Analysis of shock motion in STBLI using direct numerical simulation data. *J. Fluid Mech.* **594**, 71–83.

XIE, Z. T. & CASTRO, I. P. 2008 Efficient generation of inflow conditions for large-eddy simulation of street-scale flows. *Flow, Turbulence and Combustion*, **81**(3), 449–470.